CHARACTERISTICS OF OCEAN-REFLECTED SHORT RADAR PULSES WITH APPLICATION TO ALTIMETRY AND SURFACE ROUGHNESS DETERMINATION

12

N73-15381

Lee S. Miller and George S. Hayne
Research Triangle Institute
Research Triangle Park, North Carolina

The purpose of this paper is to summarize our current work related to geodetic altimetry. Special emphasis is placed on the effects of pulse length on both altimetry and sea-state estimation. Some discussion is also given of system tradeoff parameters and sea truth requirements to support scattering studies. The paper first considers the problem of analyzing signal characteristics and altimeter waveforms arising from rough surface backscattering.

1.0 Rough Sea Effects on the Altimeter Backscattered Waveform

The most frequently used analytical model for describing ocean surface waveform effects on the altimeter signal is based on linear scattering theory [1-3]. With this model, the scattering process may be conceptualized as resulting from the double convolution of the transmitted pulse, the sea scattering impulse response, and the altimeter system impulse response, as shown in Fig. 1. The sea surface ensemble average, temporal impulse response f(t) for this model may be written, for pulse lengths up to a few microseconds, as [2]

$$f(t) = \frac{kc}{\left(\frac{ct}{2}\right)^4} \; I(\theta,t) \int_{\frac{-ct}{2}}^{+\infty} (h-z)\, p(z)\, dz$$

where c is the velocity of light, h is satellite altitude, p(z) is the ocean wave height probability distribution as weighted by the radar observation, and $I(\theta,t)$ describes the altimeter antenna pattern.

The principal assumptions in this theory are:

(1) The radar scattering from the ocean surface occurs as though the surface contained an arbitrarily large number of spatially

stationary, independent, random scattering elements distributed on the ocean surface.

(2) The radar scattering is scalar with no polarization effects, and the return power is proportional to the incremental ocean area illuminated, appropriately weighted by antenna beamwidth and geometry factors. Radar cross-section variation with angle is assumed to be negligible over the antenna beamwidth expanse.

(3) The effect of ocean surface roughness on the radar waveform is derived based upon a model which assumes that the reflection statistics are known a priori. The scattering function is assumed to be distributed in the vertical coordinate in a manner describable by probability density function p(z).

(4) It is assumed that the convolution operations can be interchanged with the waveform expectation operation, for ensemble or mean waveform computations.

The greatest unknown in this model is considered to be the effective wave height probability distribution p(z) and its relationship to the true ocean surface. The work of Yaplee et al. marks the first occasion for which experimental data is available concerning p(z) and the ocean wave height distribution simultaneously [6]. The oceanographic unknowns and statistical complexities of the problem appear to preclude a derivation of the p(z) distribution based on oceanographic variables in the foreseeable future [4]. Longuet-Higgins has given an analysis based on a facet scattering model and use of idealized ocean surface statistics [5]. Attempts to extend this work have been unsuccessful for the following reasons: The two dimensional problem involves ocean spectral moments m_{ij} such as

$$m_{44} \triangleq \int\int K_x^4 \, S(k_x,k_y) \, dk_x \, dk_y$$

in which $S(k_x,k_y)$ is the directional wave number spectrum. This integral can be shown to be unbounded for frequently used ocean spectral models [4]. Secondly, joint probability distributions of the ocean surface are not known.

In regard to the other assumptions, experimental tests of correctness of the overall model will be available from the Skylab waveform experiment. Item 4 above may be verified and the model improved for particular system configurations via Monte Carlo simulations presently being conducted by the authors or through a time-variant linear system formulation of the problem.

A problem area that is closely associated with waveform modeling is that of sea-state bias. The term "sea-state bias" is used herein to denote differences between mean sea level as sensed by the altimeter and geometrical mean sea level. That is, any discrepancies that arise in the altitude processing operation that results from differences in the radar observed $p(z)$ and the true wave height distribution $q(z)$ will appear as a bias in the altitude measurement. Estimates of sea state bias were first made by Pierson based upon the bias effect arising solely from skewness in $q(z)$ and by equating $p(z)$ to $q(z)$ [1]. (It should be noted that such a model results in larger biases for shorter pulse length altimeters [2]). In the following section we examine the experimental data recently published by Yaplee et al., and present a rationale for the essential time displacements he observed between $p(z)$ and $q(z)$.

2.0 Sea State Bias and Radar Observed Wave Height Distribution

The experimental data recently published by Yaplee et al. on their nanosecond radar measurements shows sea state bias to be much larger than previously estimated for low sea states. While the data base is quite limited and the results are preliminary, it is of interest to examine Yaplee's data in terms of its inferences regarding radar backscattering. On physical grounds we expect the radar wave height profile to be a distorted version of the ocean wave height profile, and the data of Yaplee et al. may be interpreted as indicating that this distortion appears mainly as a relative time shift between the two distributions as shown in Fig. 2. In the following we find that this apparent displacement can be accounted for, within experimental error, by assuming that $p(z)$ is a weighted replica of $q(z)$.

Yaplee's experimental configuration is that of a beamwidth limited exploration of the sea surface. The surface area investigated is that due to an essentially collimated beam. The data we wish to discuss is contained in Figures 9-12 of Ref. 6.

In attempting to model rough sea effects, it has been universally assumed that the cross-section is a function of the area of the ocean surface illuminated. There can be not large quarrel with this assumption; however, there is presently no basis for assuming that the scattering cross-section per unit area is independent of height above "mean sea level", (MSL), and only a function of the projected area. Figures 9 and 10 of [6] can, in fact, be interpreted as showing that radar cross-section of the ocean surface over the range of wave heights increases linearly with increasing distance below the wave crests. For these figures, the slope of the linear increase is approximately

$$m = \frac{.185}{\sigma} \qquad \text{for Figure (9) (calm seas)}$$

$$m = \frac{.141}{\sigma} \qquad \text{for Figure (10)(21 knot wind)}$$

where σ is the rms wave height.

If we take the geometrical centers of the delay expanse in these data as identifying MSL, then the variation of radar cross-section about MSL is given by

$$1 - m\frac{z}{\sigma}$$

where z is measured positive about MSL. Assume for the moment that p(z) can be interpreted as the product of two terms:

$$p(z) = h(z).q(z)$$

where h(z) is the z variation of radar cross-section per unit area and q(z) is the probability of finding a surface element z meters about MSL. We might expect that q(z) may well be of the form proposed by Pierson and Mehr [1]. However, for the conditions at the time that Yaplee's data were taken (calm sea-swell), the skewness parameter λ is expected to be quite small. Accordingly, we take

$$q(z) = \frac{1}{\sqrt{2\pi\sigma^2}} \exp - \frac{z^2}{2\sigma^2} .$$

We are concerned, therefore, with the behavior of p(z) as implied by Yaplee's data.

Three curves are shown in Fig. 3.

$$p(x) = h(x).q(x) = \frac{1}{\sqrt{2\pi}} [1-mx] \exp(-\frac{x^2}{2}) \qquad \text{weighted Gaussian}$$

$$q(x) = \frac{1}{\sqrt{2\pi}} \exp(-\frac{x^2}{2}) \qquad \text{true Gaussian}$$

$$p(x + .175) = \frac{1.02}{\sqrt{2\pi}} \exp(-\frac{(x - .175)^2}{2}). \qquad \text{displaced Gaussian}$$

where m was taken to be 0.115.

Comparison of these curves indicates that p(x) is displaced from the wave height distribution, just as is the data in Yaplee's Figure 11 (see Fig. 2). The x variable used in these calculations is the height normalized by the rms wave height. From Yaplee's Figure (11), we find that the rms wave height expressed in nanoseconds is 1.725. The delay between the peaks of the two curves [p(x) and q(x)] is therefore .3 nanoseconds. The third curve--merely the Gaussian curve shifted and re-normalized--shows the extent to which p(x) can be approximated by a shifted Gaussian curve. The reader may satisfy himself that Yaplee's radar data in Figure 11 can be obtained by simply shifting the wave staff data .3 nanoseconds to the right.

This discussion suggests that one possible explanation of the shift in Yaplee's radar curve is a simple height dependence of the scattering cross-section as provided by the h(z) term. Note that for this sea condition, a skewness parameter λ cannot support the data--it would require a λ of approximately .37 for a calm sea! Note further that the skewness correction to a Gaussian curve is essentially a cubic $[1 + \frac{\lambda x}{6} (x^2 - 3)]$ and that there will be three places at which the Gaussian intercepts the composite curves. Yaplee's data show only one intersection between the radar and wave staff data--which would be expected if the radar data are just shifted wave staff data. This may be taken as further proof that for this sea condition the wave staff data are essentially Gaussian.

Under conditions of a true wind-driven sea, one might expect that the variation of radar cross-section with height above mean sea level may

change. Possibly "m" might decrease. With increasing wind speed, one might also expect the value of λ, the skewness parameter in the wave height distribution, to increase. The overall effect on sea surface bias will still be contained in the formula for p(z)

$$p(z) = \frac{1}{\sqrt{2\pi}} \left[1 + \frac{\lambda}{6}\left(\frac{z}{\sigma}^3 - \frac{3z}{\sigma}\right)\right]\left[1 - m\,\frac{z}{\sigma}\right] \exp\left(-\frac{z^2}{2\sigma^2}\right)$$

These detailed variations with wind speed and sea state are not known and must be measured. In any event, Yaplee has made a clear case for the inclusion of a term which reflects the increasing radar cross-section per unit area with increasing distance below the wave crests.

3.0 Selection of GEOS-C System Parameters Relative to a Sea-State Experiment

In this section we discussed the problem of estimating ocean surface roughness using information available from altimeter normal incidence waveforms. Referring back to Fig. 1, in such an experiment an attempt would be made to measure the width of the p(z) distribution (i.e., its rms value) and thereby infer the surface roughness parameter in the wave height distribution q(z). In order to implement such an experiment, it is necessary to sample a number of points on each incoming waveform and subsequently average (either in the satellite or on the ground) the sample values to extract the ensemble average. The mean waveform can then be examined to derive surface roughness estimates. If it is assumed that p(z) is a symmetrical bell shaped distribution, in an idealized case the sample and hold spacing could be as great as one-half the transmitted pulse length. If it desired to obtain data on the p(z) distribution, then a rather dense collection of sample and hold values would be needed. The problem areas in such an experiment are: 1) Given that satellite constraints place a limit on the sample and hold spacing and signal-to-noise ratio available, and that sea state sensitivity is greatest for short pulses; then an optimum pulse length may exist for sea state measurement. 2) The number of waveform samples available per measurement interval is limited by the homogeneity of the ocean surface during the experiment, the statistical nature of the received signal and other

system constraints. These factors may be seen from an examination of Figs. 4 and 5, which comprise computed* mean waveforms as a function of sea state. These figures show square-law detected waveforms for a matched receiver (i.e. an IF bandwidth equal to the reciprocal of the pulse length) for both 10 and 25 n.s. pulse lengths. RMS surface roughness values are shown on these figures for an assumed Gaussian p(z). To convert these values to significant wave height ($H_{1/3}$) requires multiplication by a factor of four [1].

Figures 4 and 5 also show the one-sigma confidence bounds for the magnitude fluctuations on a waveform containing 1000 sample cases. Based upon an input signal comprising a square-law detected narrow-band, time-varying Gaussian signal, the rms deviation of a sample function about the distribution mean is

$$\sigma_y = \frac{\sqrt{2}\,\sigma_x^2}{\sqrt{n}}$$

where y is the detected process and y the input process. For this model the output will be chi-squared distributed (single degree of freedom) and the average value of y is

$$\bar{y} = \sigma_x^2.$$

This distribution will be modified to some degree, by the presence of the post-detection filter. Our recent work has shown the filter to produce significant departures from the chi-squared distribution for filter bandwidths of approximately the "matched filter" condition. Figure 7 contains a histogram of the filtered distribution, based on simulation results. It shows a standard deviation of very nearly one-half that of the chi-squared distribution. Adding this factor to the above result gives a vertical error component σ_v of

$$\sigma_v = \frac{\text{waveform ensemble average}}{\sqrt{2n}}$$

*These data have been computed by both closed form and hybrid computers simulations; as verification of the interchange of ensemble and convolution operations.

where the waveform ensemble average is taken to be the value of the true mean waveform at the point of interest. For example, σ_v will be $1/\sqrt{2n}$ at the peak of the normalized mean waveform; or $\pm$ 2.2% of the peak for n = 1000.

Figure 6 is a graph of the relative sensitivity of the 10 and 25 nanosecond pulse length altimeters. These data are a re-plotted version of the information contained in Figs. 4 and 5. Note that the shorter pulse length increases sensitivity to the lower sea states.

In summary, the uncertainty in measuring surface roughness, for seas in the range of 1-2 meters rms, for the 25 ns pulse length is ~ 0.2 meter rms for a one second average of 1000 pulses. Table I gives other estimates.

Table I

Estimated uncertainty in measuring surface roughness for a 10 or 25 ns pulse lengths.

Sea Roughness Uncertainty (1-2 rms seas)				
Averaging Period Sec.	25 ns		10 ns	
	rms	$H_{1/3}$	rms	$H_{1/3}$
1	0.21 meters	0.84 meters	0.14	0.56
5	.07	.28 meters	.045	.18

The timing error component in the waveform measurement, which relates to sample and hold jitter is neglected in the above discussion for the following reasons. Assuming that the sample and hold circuits follow the output of a split gate tracker, this error will be approximately 3.6 ns for n = 1000, SNR = 10 db, T = 10 ns and for a tracker bandwidth of 10 Hz (bandwidth is related to orbit eccentricity) [7,15]. If instead the sample and hold circuits are held stationary during the sea-state experiment interval, and adequately spaced to define the mean waveform, this error component will be approximately 14 ns for an orbit ellipticity of 1.05 and for a 1 second averaging interval. As the third option, the sample and hold timing could be programmed, based on orbit parameters or tracker data, thereby reducing

this error component to a fraction of the vertical error. This added complexity appears necessary except for highly circular orbits.

4.0 Altitude Measurement Considerations

At the present time it appears that GEOS-C will utilize a pulse compression mode, which in turn may permit use of pulse lengths as short as 10 n.s. Considerable emphasis has been placed on a 10 n.s. system in past program meetings and the purpose of this section is to briefly indicate other system considerations.

Previous system error analyses have shown that the largest random, instrument error in the altitude measurement is likely to be altitude noise [2,7,8,9]. Based on a pulse repetition frequency (prf) which provides independent waveform samples, the random altitude error σ_a is given by [15]

$$\sigma_a = \frac{0.15\tau}{\sqrt{\frac{prf}{\pi\beta_L}}} \sqrt{\frac{7}{8} + \frac{6}{SNR} + \frac{8}{(SNR)^2}}$$

where β_L is the 3db loop bandwidth, τ is the pulse length in nanoseconds, and SNR is signal-to-noise ratio. For high signal-to-noise ratios, this expression may be approximated as

$$\sigma_a = \frac{.14\tau}{\sqrt{\frac{prf}{\pi\beta_L}}} .$$

As a simple tradeoff situation, assume that it is possible to use an altimeter that either (a) operates at an unambiguous prf of 100 pps and with τ = 10 n.s., or (b) uses an ambiguous prf of 1,000 pps (which necessitates an acquisition mode) and a pulse length of 25 n.s. Use of the above equation shows that the 25 n.s. system will produce a lower σ_a value. Other levels of comparison are possible. If both (a) and (b) operate at an ambiguous prf based on the doppler criterion, σ_a can be shown to be proportional to pulse length to the

three-fourths power. If it is further assumed that the signal pulse signal-to-noise ratio decreases from 10 db to 5 db, the first equation above may be evaluated to show that

$$\frac{\sigma_a(10\text{ n.s.})}{\sigma_a(25\text{ n.s.})} \simeq \left(\frac{\tau_{10}}{\tau_{25}}\right)^{3/4} \sqrt{\frac{\frac{7}{8} + \frac{6}{SNR(10)} + \frac{8}{SNR^2(10)}}{\frac{7}{8} + \frac{6}{SNR(25)} + \frac{8}{SNR^2(25)}}} \simeq 0.8$$

and the 10 n.s. system gives an improvement of $\sim$ 20%.

The purpose of this discussion is to point out the fallacy in assessing altimeter performance solely on the basis of pulse length; careful consideration must also be given to satellite hardware constraints affecting average transmitter power, complexity of sample and hold circuits, logic clock rates, degree of on-board processing available and so forth.

5.0 Ground Truth Needs for a σ^o Experiment

It is often stated that normal incidence, centimeter r-f wavelength scattering is dominated by the short wavelength or capillary range of the ocean spectrum. This statement derives from series approximations or asymptotic expansions of the physical optics scattering integral, in which σ^o is found to be proportional to the mean-squared slope of the ocean surface [10]. This slope dependency coupled with use of popular models of the ocean spectrum forms the basis for this assumed capillary dependency. The work to be summarized below examines in detail the question of what ocean wavelength range dominates the physical optics scattering integral for a Phillips type of spectrum; this question is important in its implications concerning sea truth measurements necessary for validating a σ^o experiment.

The near-normal incidence dependence of σ^o on ocean surface parameters is generally agreed to depend on the integral

$$I_{SC} = \int_o^\infty \int_o^{2\pi} e^{j2\bar{k}_o r\cos\phi\sin\theta - 4\bar{k}_o^2 h_m^2 \cos^2\theta[1-\rho_n(r,\phi)]} r dr d\phi$$

where

$\bar{k}_o$ = rf wavenumber

h_m^2 = mean-squared height of the ocean waves

θ = angle of incidence (measured from the normal to the mean ocean surface)

$\rho_n(r,\phi)$ = normalized surface height correlation function.

In order to verify the relationship between σ^o and sea state, it is necessary to measure the mean-squared ocean height and also obtain the ocean height correlation function, simultaneously with σ^o. One approach to determining $\rho_n(r,\phi)$, the normalized height correlation function, is to measure the ocean height spectrum $S(k,\psi)$ and subsequently to compute $\rho_n(r,\phi)$ from the transform relation,

$$\rho_n(r,\phi) = \frac{1}{2\pi h_m^2} \int_0^{\infty} \int_0^{2\pi} S(k,\psi)\ e^{jkr\cos(\phi-\psi)}\ k\,dk\,d\psi$$

The spectral form chosen for this study is primarily based on the asymptotic behavior of the Phillips equilibrium spectrum [13]. The low wavenumber range, for which the analysis is less sensitive, is based on experimental data given in [15]. The spectral form is

$$S_a(k) = \beta \frac{k^5}{(k^2 + a^2)^4}$$

where $\beta = 4.05 \times 10^{-3}$, $a^2 = 1/(300\ v^4)$, v is the wind speed which has dimensions in knots and k has dimensions in centimeters. These values equate the mean square height derived from $S_a(k)$ to that of the Pierson-Moskowitz spectrum. In accordance with most scattering analyses, the spectrum is taken to be isotropic [10].

The correlation function $\rho_n(r)$ derived from $S_a(k)$ is given by

$$\rho_n(r) = ar\left[-arK_o(ar) + \left(1 + \frac{a^2r^2}{8}\right) K_1(ar)\right]$$

where $K_o(ar)$ and $K_1(ar)$ are modified Bessel functions. A plot of $\rho_n(r)$ and the scattering integrand is shown in Figures 8 and 9. Several unsuccessful attempts were made to obtain an asymptotic expansion which would represent the σ^o behavior as a function of wind speed. The integrand plots in Figure 9 provide a graphic illustration of the difficulty associated with asymptotic techniques. The effective integration range spreads in the r parameter to the extent that it is difficult to obtain a valid point expansion. The scattering integral I_{SC} is shown in Figures 10 and 11 as a function of wind speed and angle of incidence for an r-f wavelength of 3 cm. These figures also show a comparison with experimental data from Ref. 11. Note that a saturation effect at the higher wind speeds is present in Figure 10.

To compute the effect of spectrum truncation on the correlation function, the upper limit on the k-integration was taken to be k_c rather than infinity, i.e.,

$$\tilde{\rho}_n(r) = \frac{1}{h_m^2} \int_0^{k_c} J_o(kr)\, S_a(k)\, kdk$$

In order to avoid a time consuming numerical integration, the following series representations for $\tilde{\rho}_n(r)$ were developed and verified;

$$\tilde{\rho}_n(r) = \frac{\beta}{2} \sum_{m=0}^{2} \frac{\left(-\frac{1}{4} r^2\right)^m b_m}{(m!)^2} + \beta\, \Phi(k_c r)$$

where for $k_c r < 1$,

$$\Phi(k_c r) \simeq 0$$

and for $\left(\frac{k_c}{a}\right)^2 > 9$ and $k_c r < 5$

$$\Phi(k_c r) = \frac{1}{k_c^2} \sum_{m=2}^{\infty} \frac{\left(-\frac{1}{4} r^2 k_c^2\right)^m}{(m!)^2 (2m-2)}$$

and finally for $\left(\frac{k_c}{a}\right)^2 > 9$ and $k_c r \geq 5$,

$$\Phi(k_c r) = \frac{r^2}{2}\left[\frac{1 - J_o(k_c r) + \left(\frac{k_c r}{2}\right) J_1(k_c r)}{(k_c r)^2} + \frac{(\gamma-1)}{2} + \frac{1}{2}\log\left(\frac{k_c r}{2}\right)\right]$$

$$+ \frac{r^2}{4}\left[\frac{2g_1(k_c r)\, J_o(k_c r)}{(k_c r)^2} - \frac{g_o(k_c r)\, J_1(k_c r)}{(k_c r)}\right]$$

The functions $g_1(k_c r)$ and $g_o(k_c r)$ are given in [14], γ is Stirling's constant and the b_m coefficients are as follows:

$$b_o = \frac{1}{3a^2} - \delta^2 + a^2\delta^2 - \frac{1}{3}a^4\delta^3$$

$$b_1 = -\log(a^2) - \frac{11}{6} + \log(\delta) + 3a^2\delta - \frac{3}{2}a^4\delta^2 + \frac{1}{3}a^6\delta^3$$

$$b_2 = \frac{10}{3}a^2 + 4a^2\log(a^2) - 4a^2\log(\delta) - 6a^4\delta + 2a^6\delta^2 - \frac{1}{3}a^8\delta^3$$

and $\delta = (k_c^2 + a^2)^{-1}$.

When k_c (the upper truncation point) was set equal to one $(cm)^{-1}$, the scattering integral I_{SC} had essentially the same value as when $k_c \to \infty$. To understand how the scattering integral behaves as a function of the spectral truncation point, it is necessary to examine $1-\tilde{\rho}(r)$ as a function of r. Figure 12 is such a plot with $k_c = 1(cm)^{-1}$ and as a function of r and wind

speed. All of the curves have exactly the same shape with a downward translation being the only effect of increasing the velocity. This fact indicates that the correlation function $\tilde{\rho}_n(r)$ is parabolic over the region of interest. The other important point to note from Figure 12 is that $[1 - \tilde{\rho}_n(r)]$ decreases almost uniformly with increasing velocity. In Figure 13, the spectrum interval from 10^{-3} - 1 $(cm)^{-1}$ was taken to represent $\tilde{\rho}_n(r)$. Here it should be noted that $[1 - \tilde{\rho}_n(r)]$ becomes independent of velocity for $v \geq 20$ knots. Since the mean-squared height continues to increase with velocity, this would imply that the scattering integral I_{SC} will exhibit a very rapid roll-off as a function of velocity for greater than 20 knots. Figure 14 shows how the scattering integral behaves when the lower spectrum truncation point is increased from zero to 10^{-2} $(cm)^{-1}$. Figure 15 shows the effect of truncating the spectrum below $k_c = 1.0$ $(cm)^{-1}$. It is most interesting that while varying the lower truncation point drastically changes the shape of the curve, changing the upper truncation point apparently only causes a level shift and not a significant change in the shape of the curve.

The computations presented here indicate that a correlation of spectrally narrow-band sea truth data and experimental values of σ^o with theoretical formulations (for near-normal incidence) will not yield good agreement. Data shown in Figure 15 indicates that sea truth data over a wavenumber range of 0.001 to 1.0 cm^{-1} will be adequate for equilibrium surface winds $\leq$ 8 knots. For higher winds, it is necessary to locate the lower truncation point at a position somewhat below the equilibrium spectral peak.

It must also be concluded that the often-used isotropic assumption is, strictly speaking, not appropriate. However, adequate oceanographic information is not available for an analysis which includes directionality. Also, current work indicates that the conclusions given herein will still hold.

6.0 Summary and Conclusions

We discussed the use of ocean surface impulse response models to obtain radar return waveform expectation values. It was assumed that the ensemble averaging and convolution operations could be interchanged, and preliminary results from our current analog simulation work support this assumption.

We distinguished between the radar-observed height distribution p(z) and the true geometric distribution q(z). Although it has usually been assumed

that p(z) and q(z) are identical, we discussed the experiment of Yaplee et al. as an example of a situation in which experimental data could be explained by assuming that p(z) and q(z) are not identical. We recommend that Yaplee's type of experimental data be obtained from as wide a range of sea conditions as possible and that, because of the difficulty of scaling from near-surface to satellite conditions, direct measurement of satellite altimeter bias be attempted using over-water radar reflectors.

We presented examples to show that sea state resolution and altitude precision did not simply vary inversely as the radar pulse length but were functions of a number of radar system parameters. It is fallacious to assess altimeter performance solely on the basis of pulse length and experimenters should instead state their needs in such terms as: extent of ocean surface over which "sea state" data can be averaged; needed sea-state resolutions and roughness range, or geographic regions of prime interest; specifications of desired altitude noise level, and time or spatial regions over which the data can be averaged. This information can then be used as input data during the altimeter system optimization phase, to select the radar system parameters and to establish different parameter tradeoffs.

Using a physical optics theory for 3 cm rf wavelength scattering at normal incidence from an ocean described by a Phillips type of equilibrium spectrum, we found that σ^o depends heavily on surface wavenumbers in the range .001 - 1.0 cm^{-1}, or ocean surface wavelengths of .06 - 60 meters, for surface winds $\leq$ 8 knots. This means that any σ^o experimentation must include acquisition of gravity wave-range spectral information, not the often-assumed capillary range, as "sea-truth" for σ^o verification. The analysis also predicts negative results for σ^o vs. wind speed experiments since a saturation effect is found in the normal incidence case, similar to the effect noted by Guinard for scatterometer geometry [11]. The Skylab σ^o experiment should provide a most valuable data base for this effect.

7.0 Acknowledgements

The authors wish to acknowledge extensive assistance from W. A. Flood in section 2.0 and Gary S. Brown in section 5.0, in addition to many helpful discussions with participants in the GEOS-C and Skylab programs.

LIST OF REFERENCES

1. Pierson, W. J., and Emanuel Mehr, "The Effects of Wind Waves and Swell on the Ranging Accuracy of a Radar Altimeter," Report on Contract No. N62306-70-A-0075, New York University, School of Engineering and Science, January 1970.

2. Miller, L. S., and G. S. Hayne, System Study of the Geodetic Altimeter Concept, Final Report, Contract No. NAS6-1829. Research Triangle Institute, March 1971.

3. Schindler, John K., Electromagnetic Scattering Phenomena Associated with Extended Surfaces, IEEE International Convention Record, v. 15, part 2, pp. 136-149, 1967.

4. A Study of the Capabilities of the Geodetic Satellite Altimeter to Measure Ocean Surface Characteristics, Final Report, Contract No. NASw-1909, by the Research Triangle Institute, April 1970.

5. Cartwright, D. E., and M. S. Longuet-Higgins, "The Statistical Distribution of Maxima of a Random Function," Proc. Roy. Soc. A-237, pp. 212-232.

6. Yaplee, Benjamin S., et al., "Nanosecond Radar Observation of the Ocean Surface from a Stable Platform," IEEE Trans. on Geoscience Electronics, Vol. GE-9, No. 3, July 1971.

7. Godbey, T. W., et al., Radar Altimetry Study, Phase II Final Report, Contract No. NAS12-683, General Electric Company, Utica, New York, January 1970.

8. Shapiro, A., and B. S. Yaplee, "Satellite Altimetry," Naval Research Laboratory Report No. 7018, February 1970.

9. Kolker, Myer, and Ephraim Weiss, Space Geodesy Altimetry Study, NASA Report No. CR-1298, March 1969.

10. Beckmann, Petr, and Andre Spizzichino, The Scattering of Electromagnetic Waves from Rough Surfaces, The Macmillan Company, New York, 1963.

11. Guinard, N. W., "The Variation of RCS on the Sea with Increasing Roughness," in Microwave Observation of the Ocean Surface, U.S. Naval Oceanographic Office SP-152, June 1969.

12. Hess, G. D., G. M. Hidy and E. J. Plate, "Comparison Between Wind Wave and Sea in the Laboratory," Journal of Marine Research, Vol. 27, No. 2, pp. 216-225, 1969.

13. Phillips, O. M., The Dynamics of the Upper Ocean, Cambridge Press, 1966.

14. Abramowitz, M., and I. A. Stegun, eds., Handbook of Mathematical Functions, pp. 482, U. S. Government Printing Office, Washington, D. C., 1964.

15. Hofmeister, E., and B. N. Kenney, "Radar Altimeter Return Waveform Sampling Study," Final Report, Contract No. NAS6-1823, by the General Electric Company, Utica, New York, May 1971.

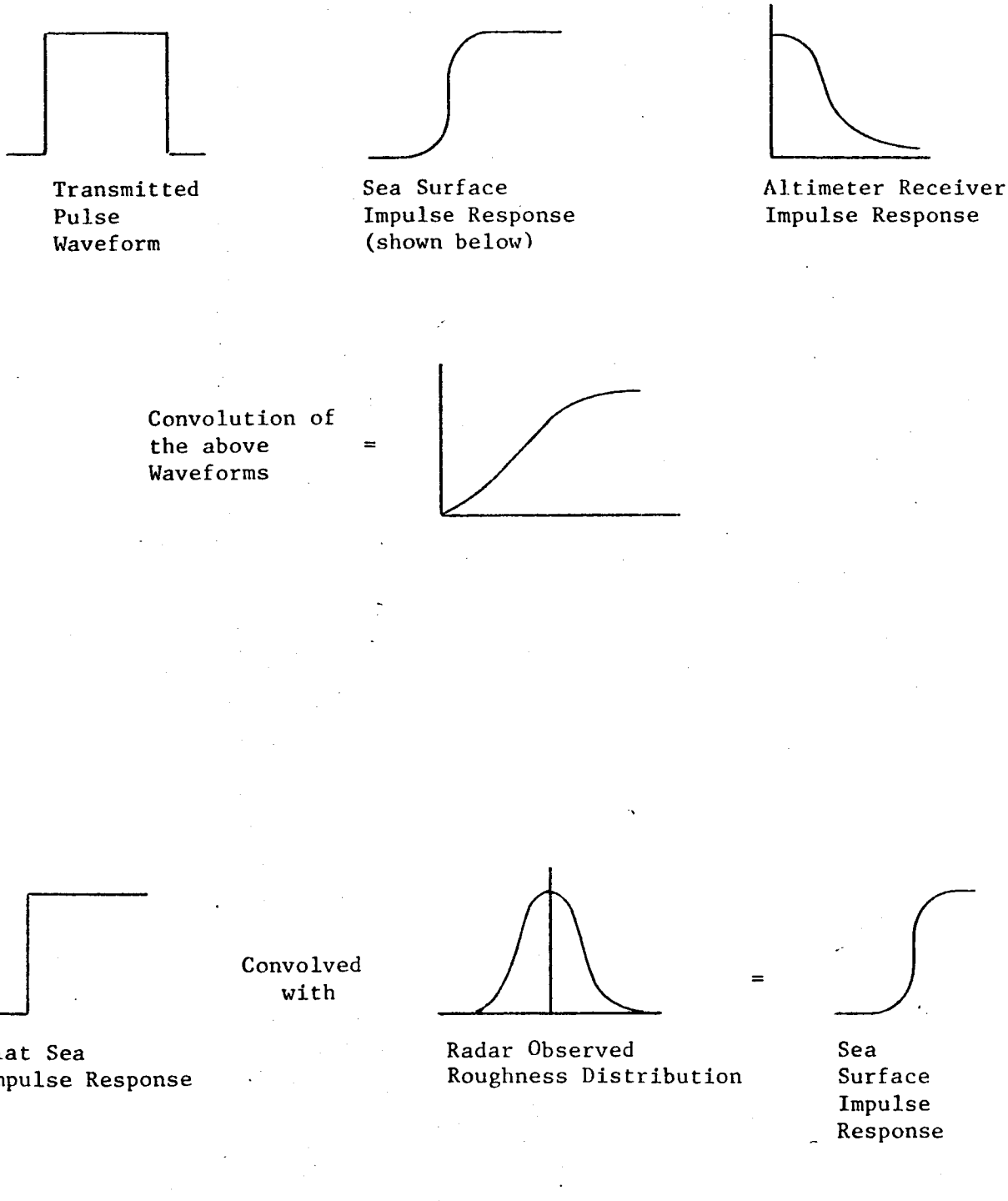

Figure 1. Altimeter Waveforms based on linear scattering theory.

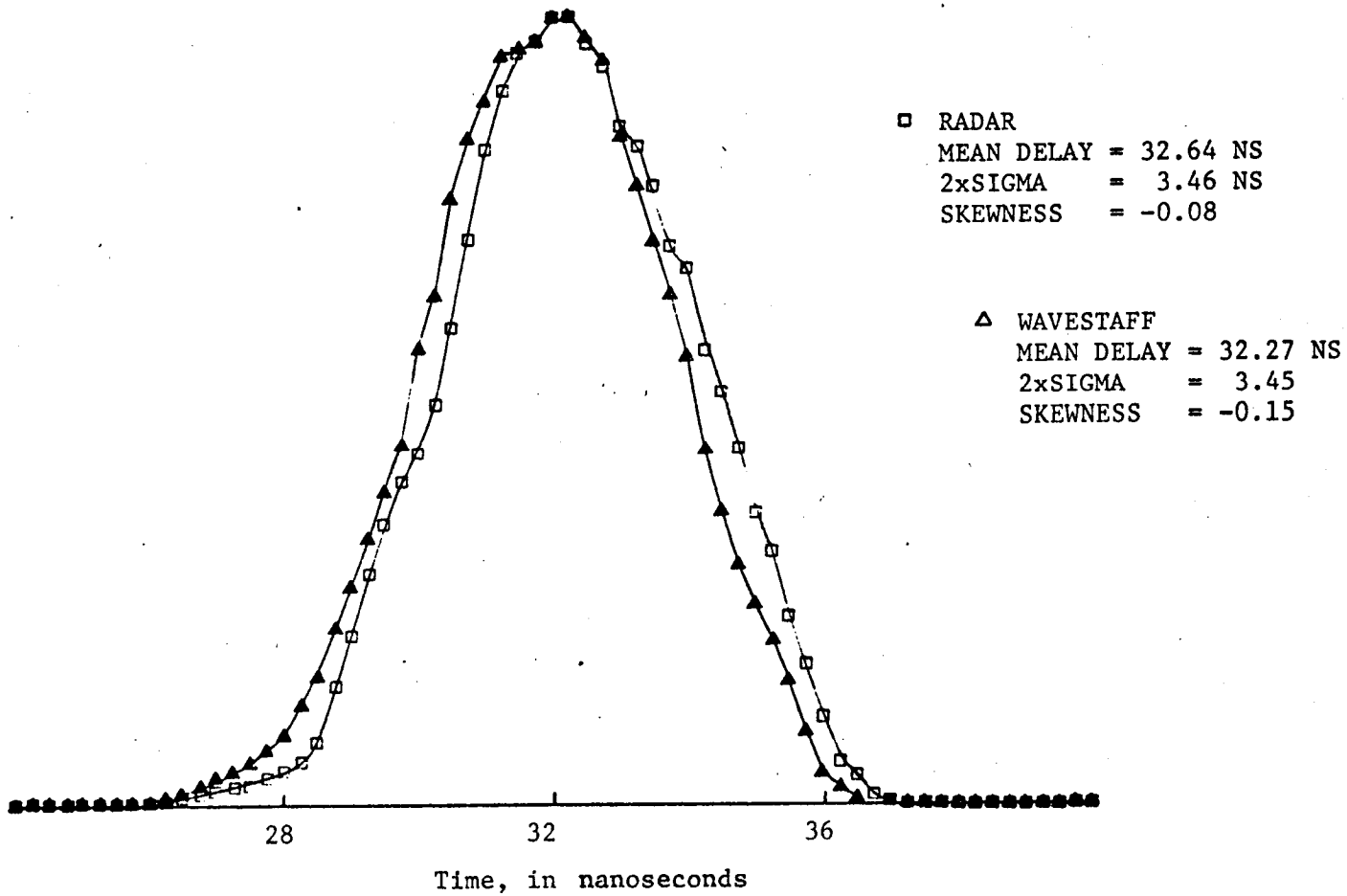

Figure 2. Comparison of Wavestaff and Radar distributions (from Yaplee et al.).

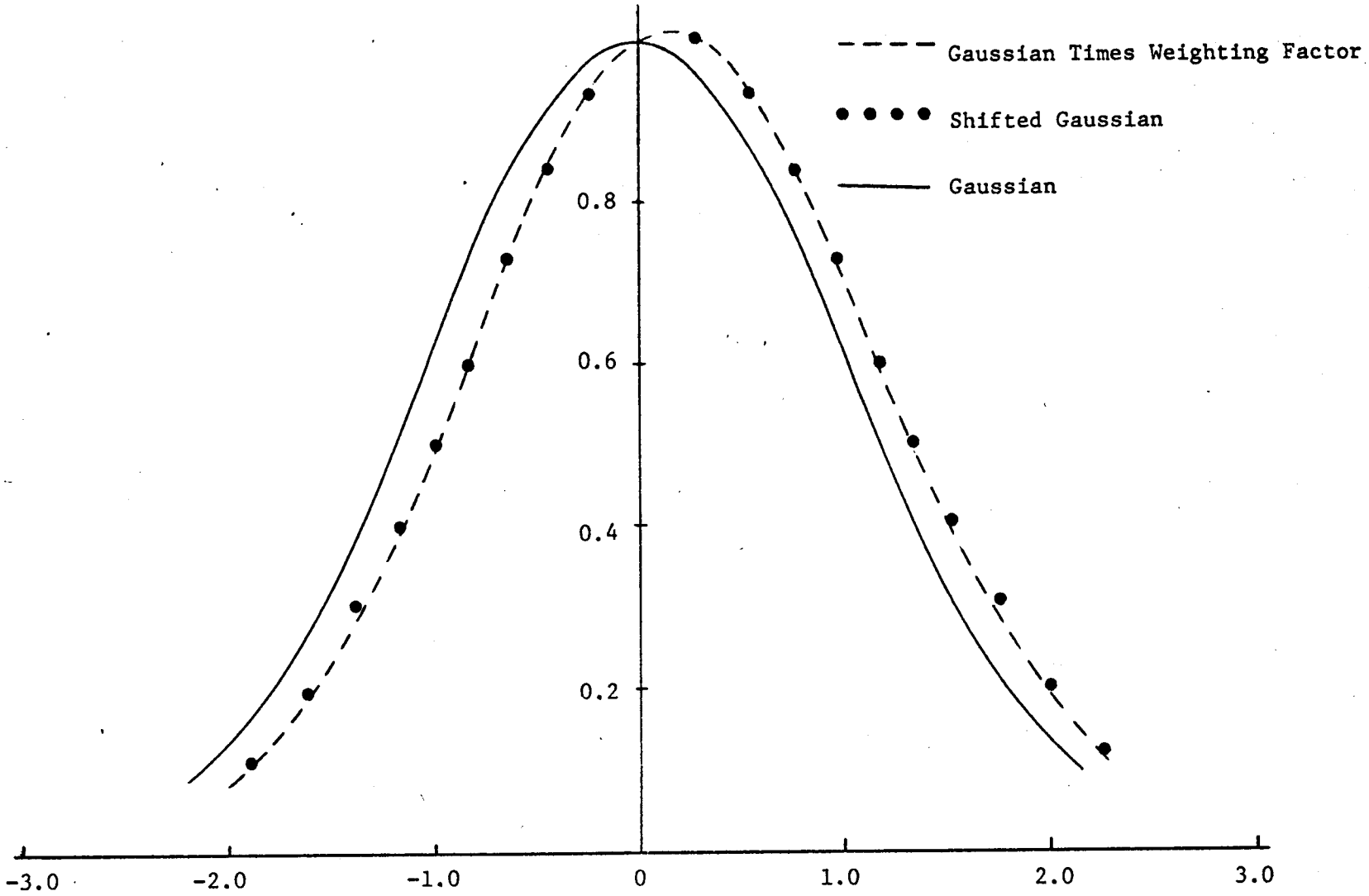

Figure 3. Comparison of linearly weighted Gaussian model of p(z) and a shifted Gaussian curve.

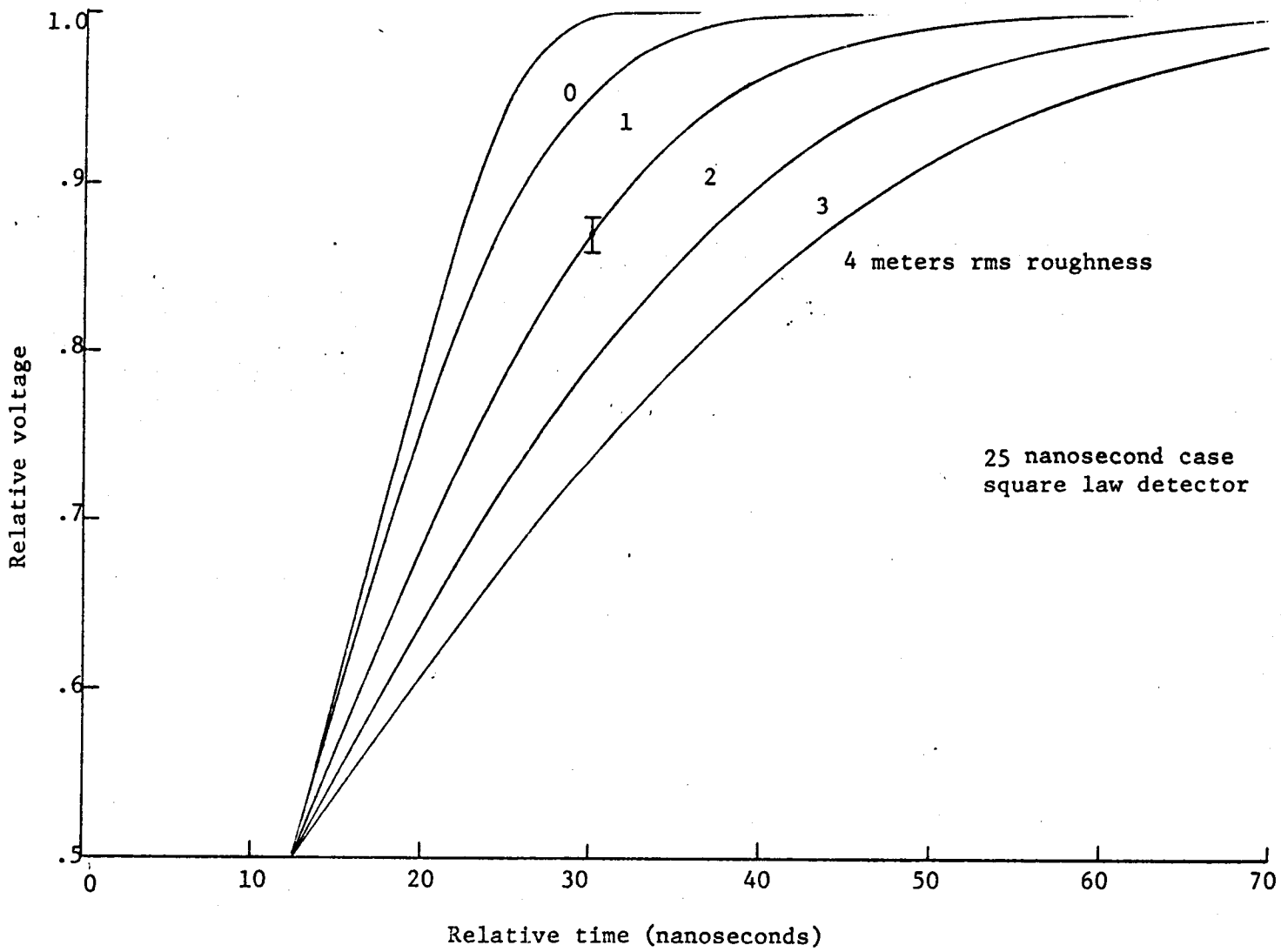

Figure 4. Sensitivity of 25 ns mean waveforms to ocean surface roughness (upper 1/2 of waveform shown).

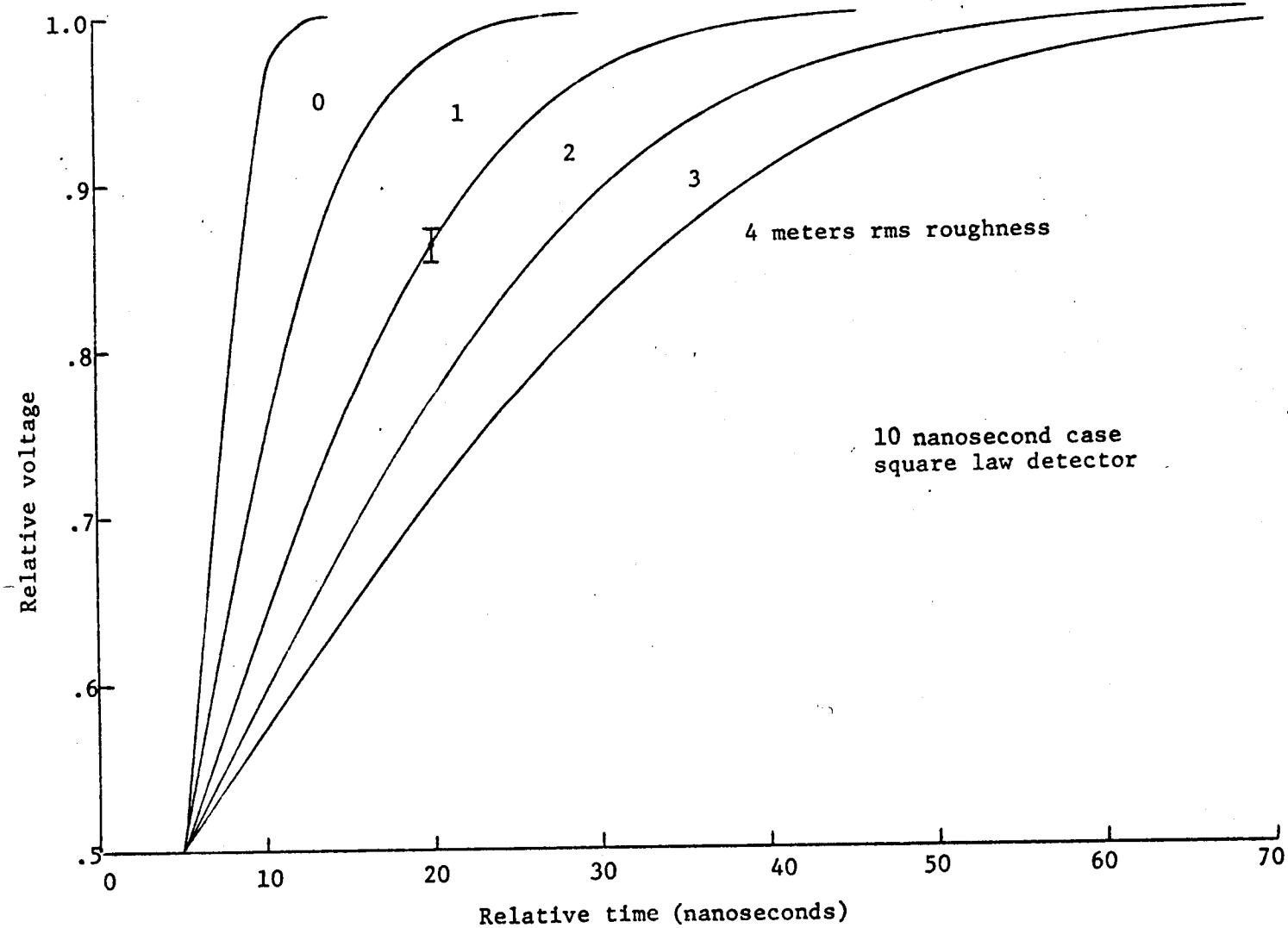

Figure 5. Sensitivity of 10 ns mean waveforms to ocean surface roughness (upper 1/2 of waveforms shown).

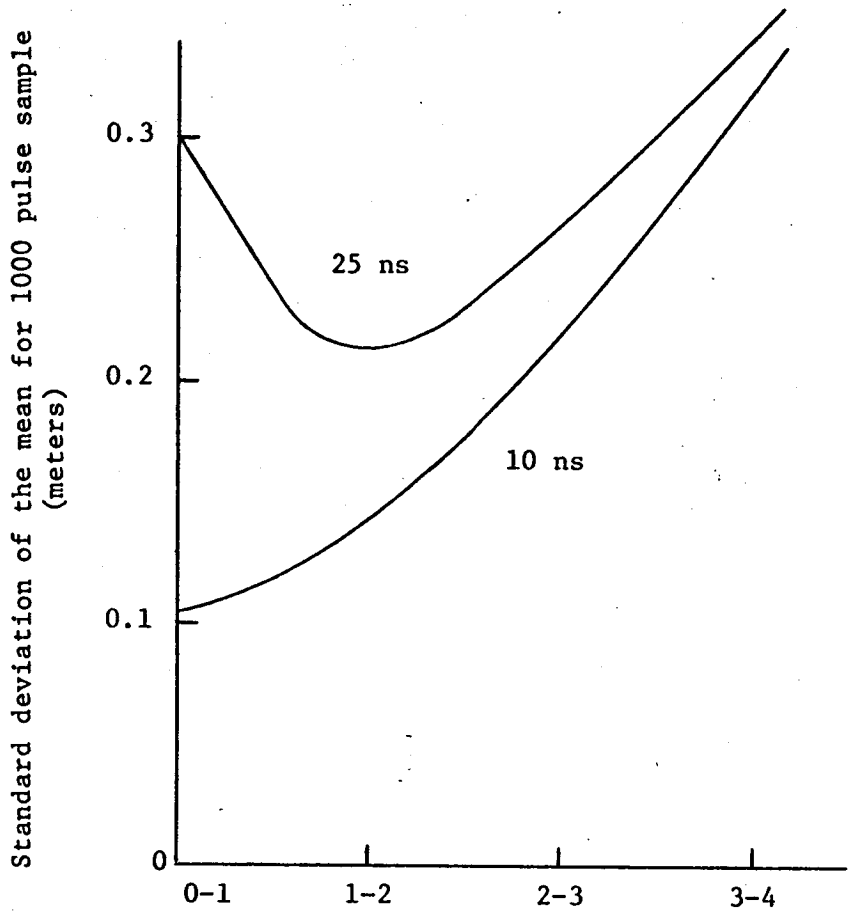

Figure 6. Calculated surface roughness measurement precision as a function of pulse length and sea conditions.

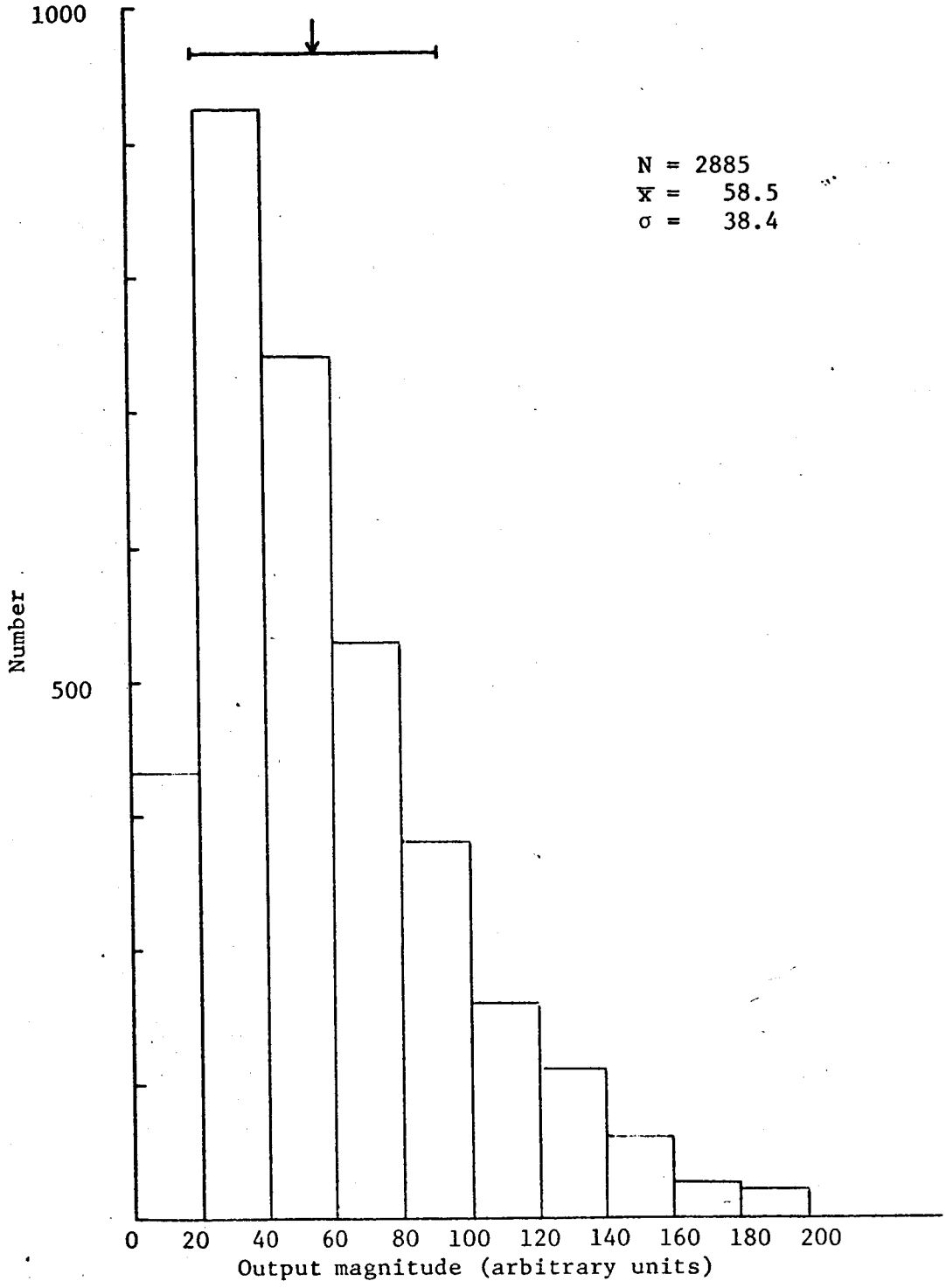

Figure 7. Histogram of simulated video filtered waveforms.

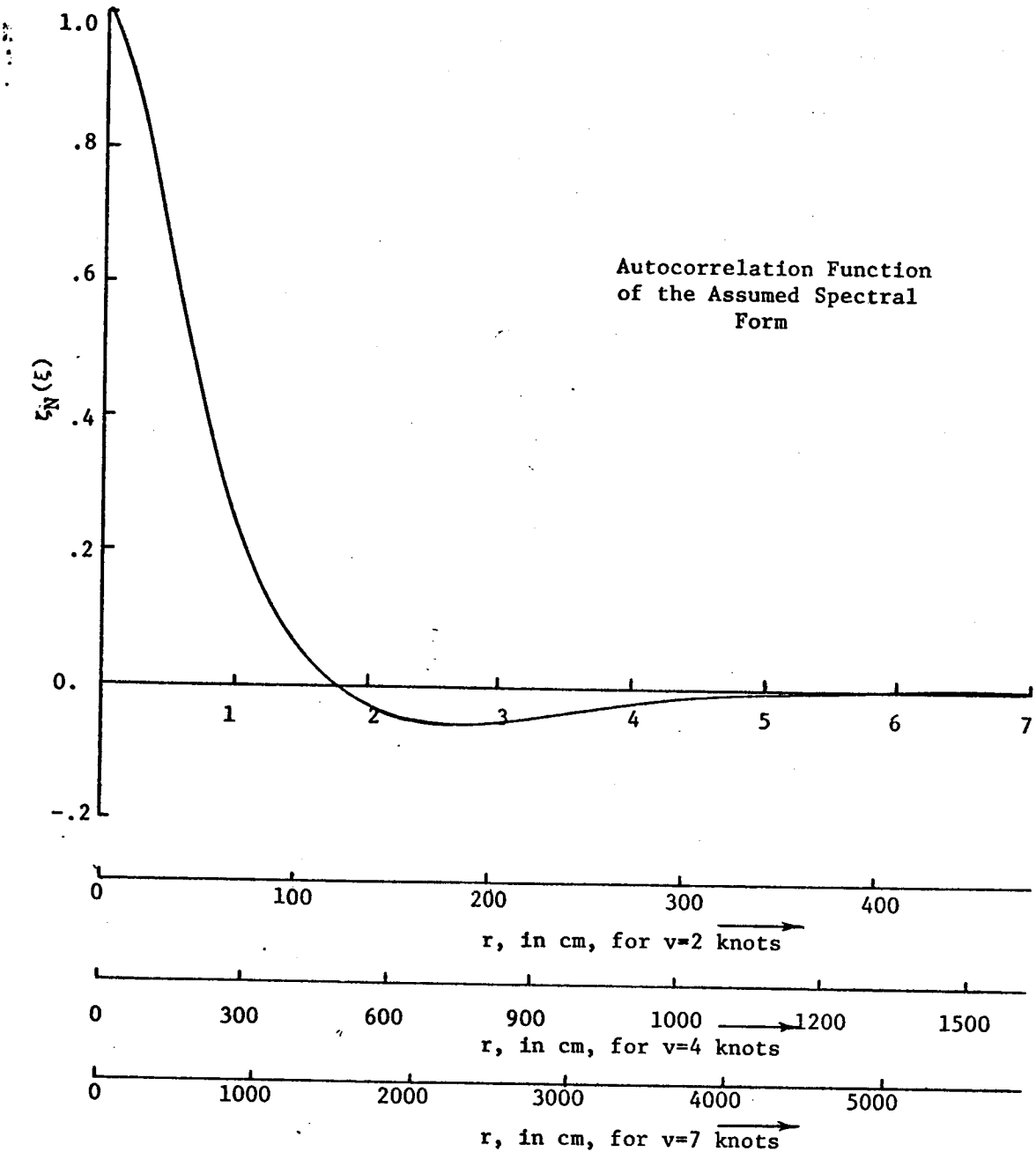

Figure 8. Normalized height correlation function.
(ξ=ar)

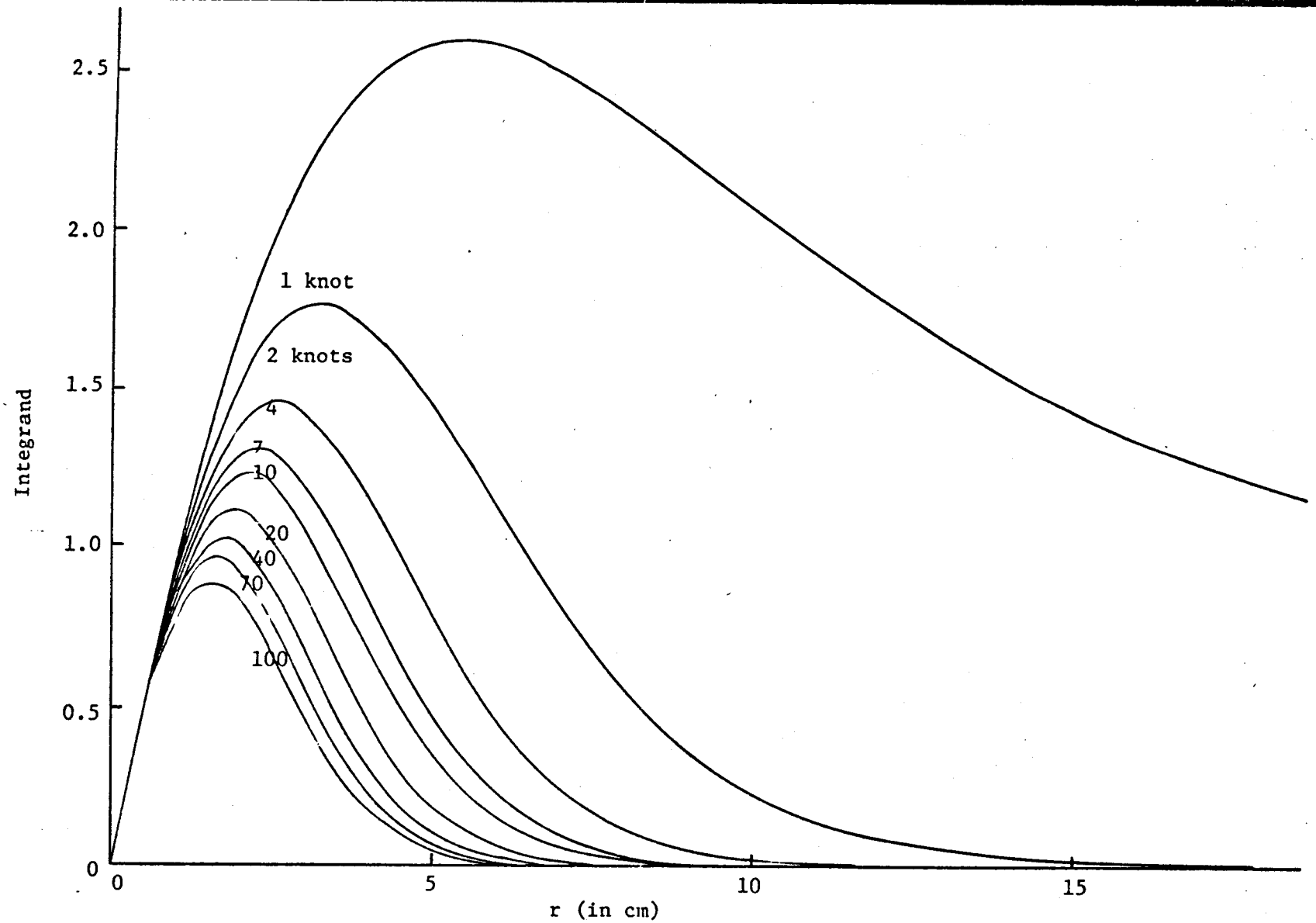

Figure 9. Behavior of the integrand of the scattering equation.

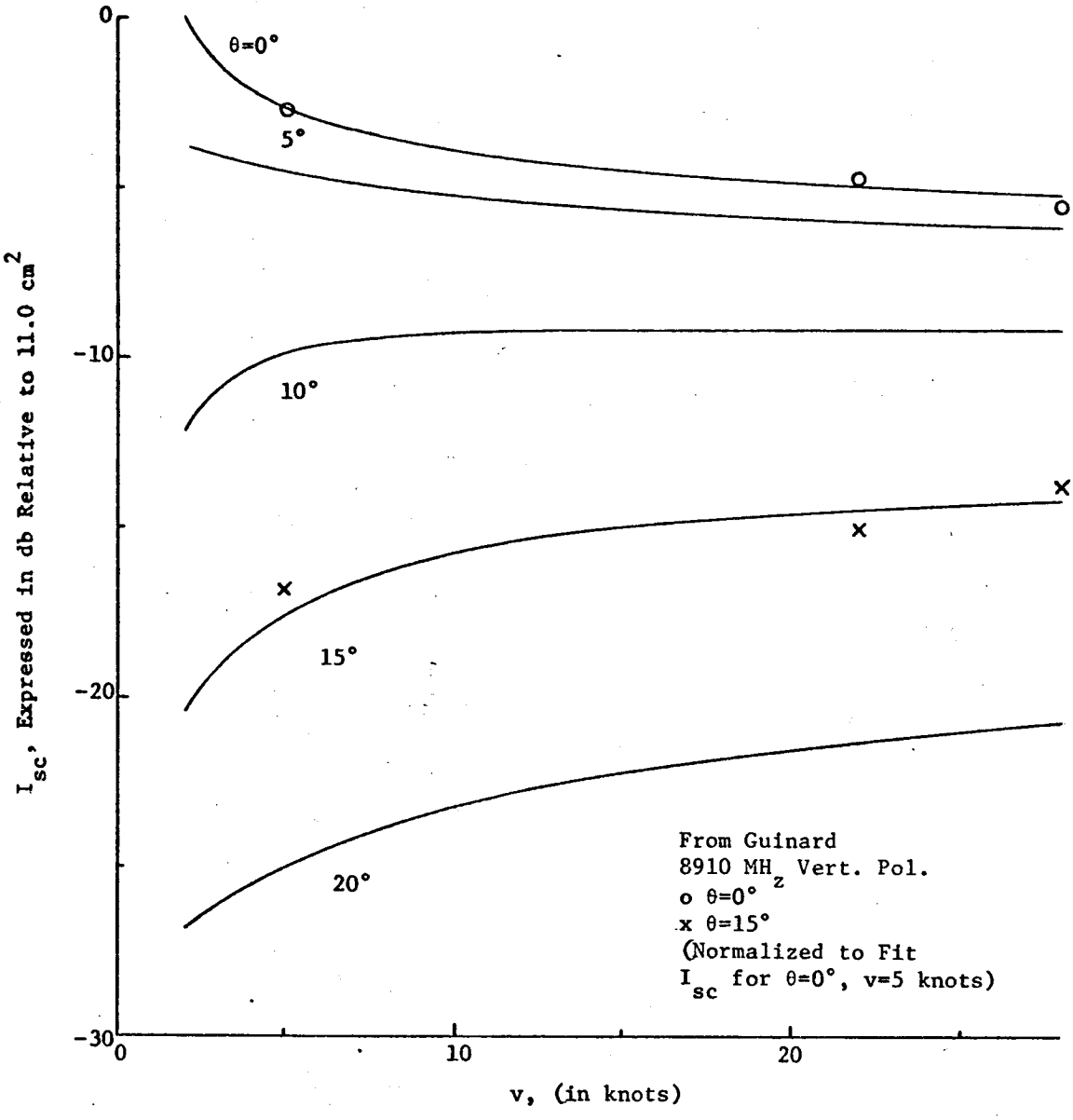

Figure 10. The scattering integral as a function of wind speed (λ_{rf} = 3 cm.).

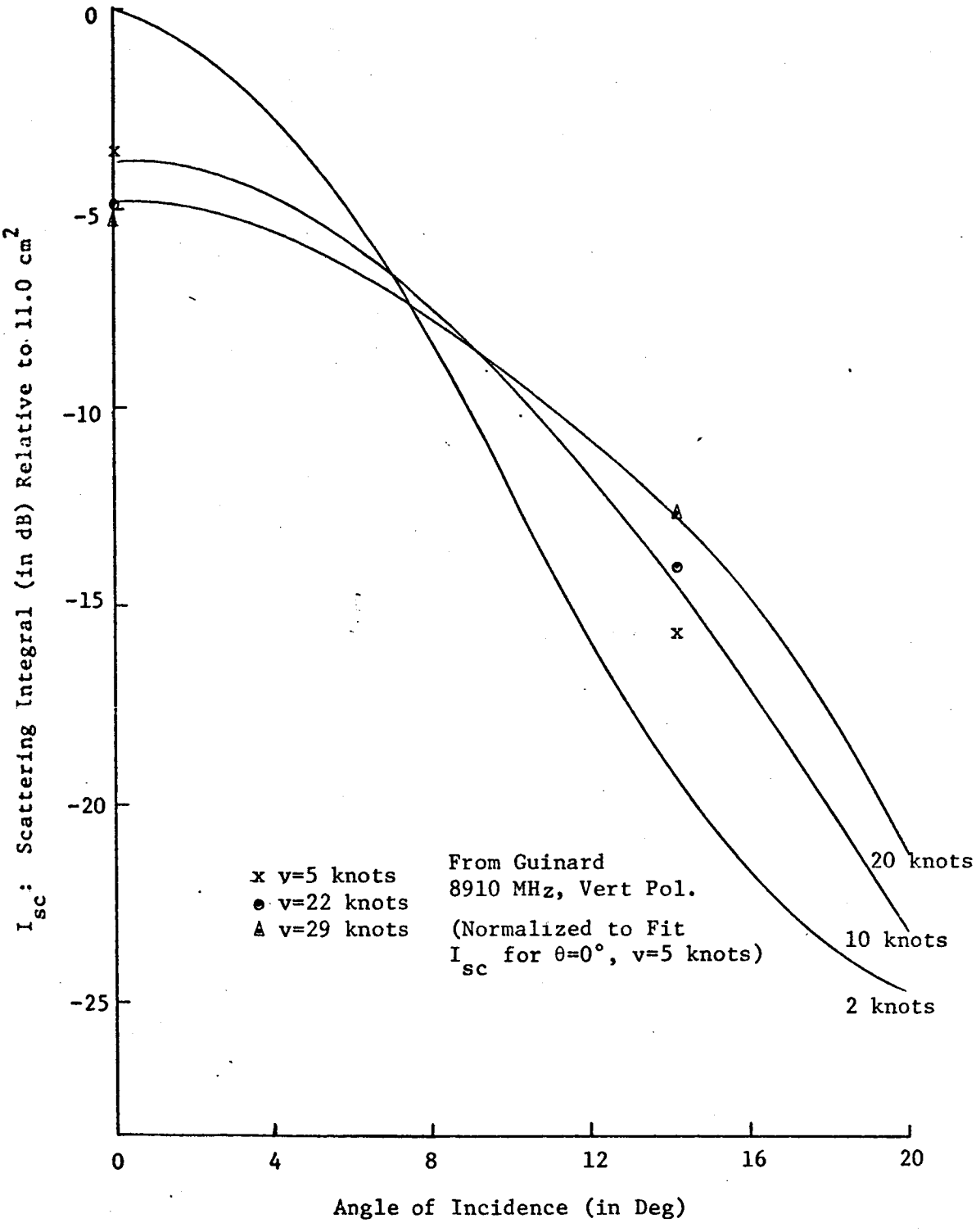

Figure 11. Scattering intergral as a function of angle (λ_{rf} = 3.0 cm)

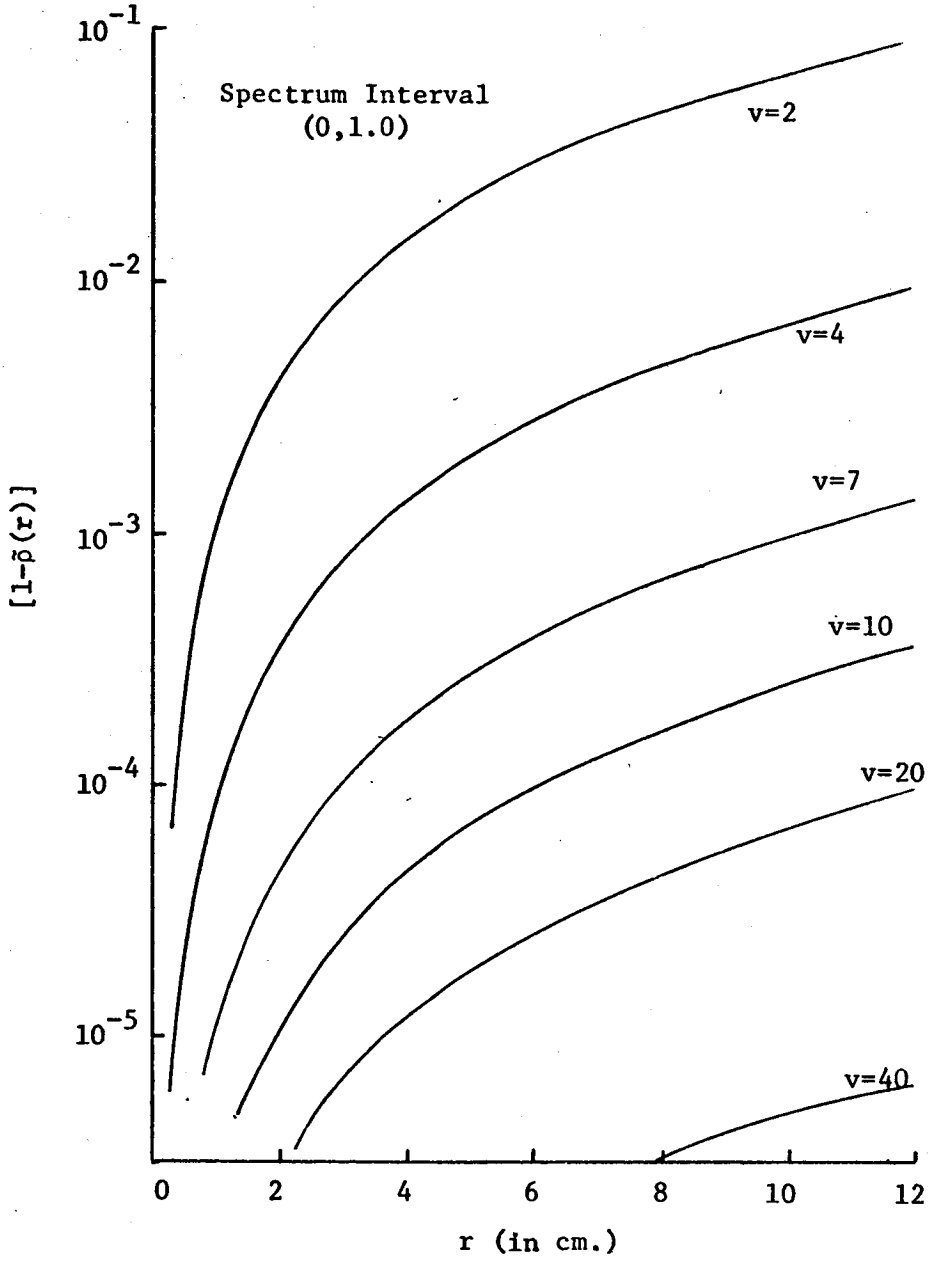

Figure 12. 1-$\tilde{\rho}$(r) as a function of r and v when the spectrum interval is (0,1.0), i.e., essentially the same as (0,∞).

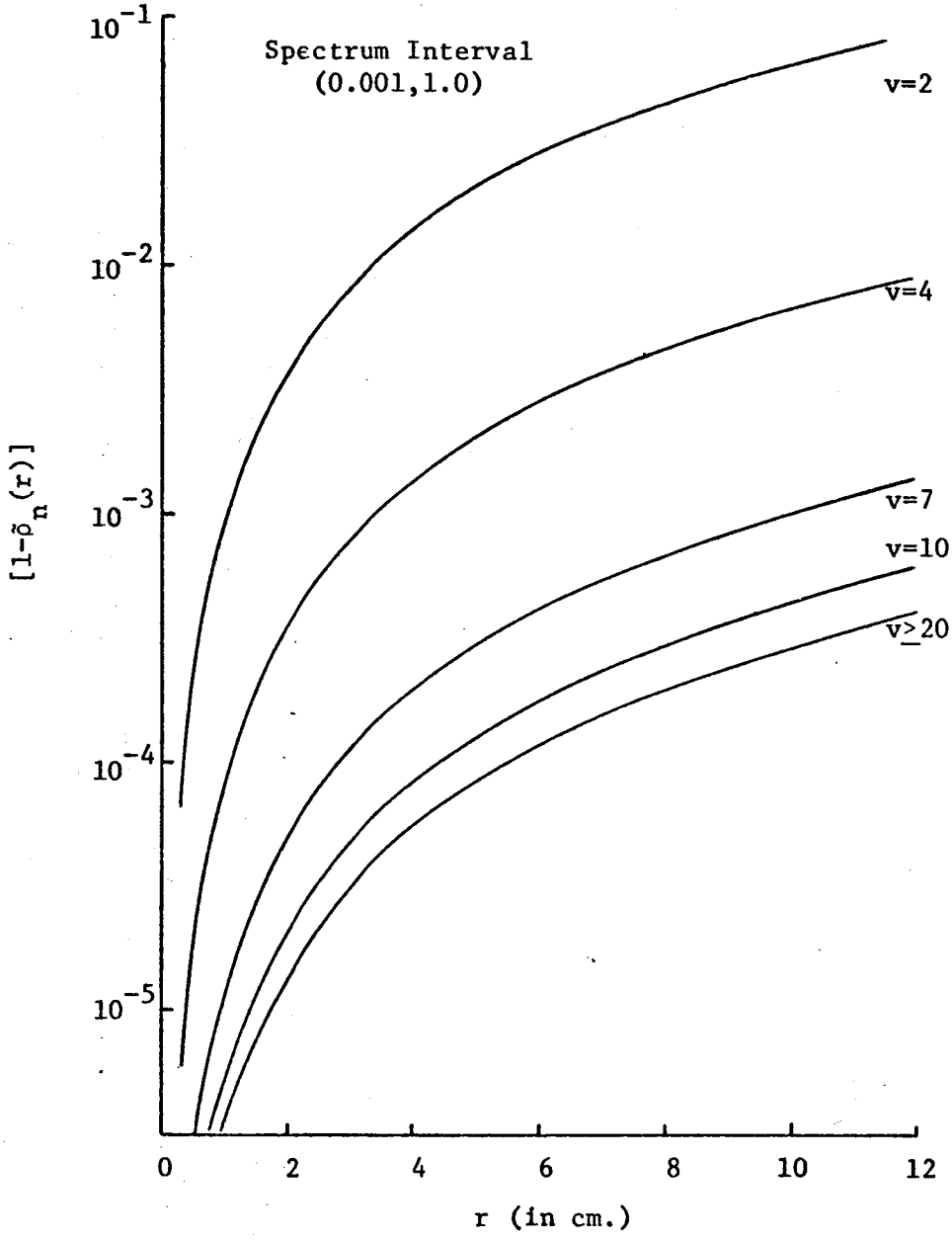

Figure 13. $1-\tilde{\rho}_n(r)$ as a function of r and v when the spectrum interval is $(10^{-3}, 1.0)$.

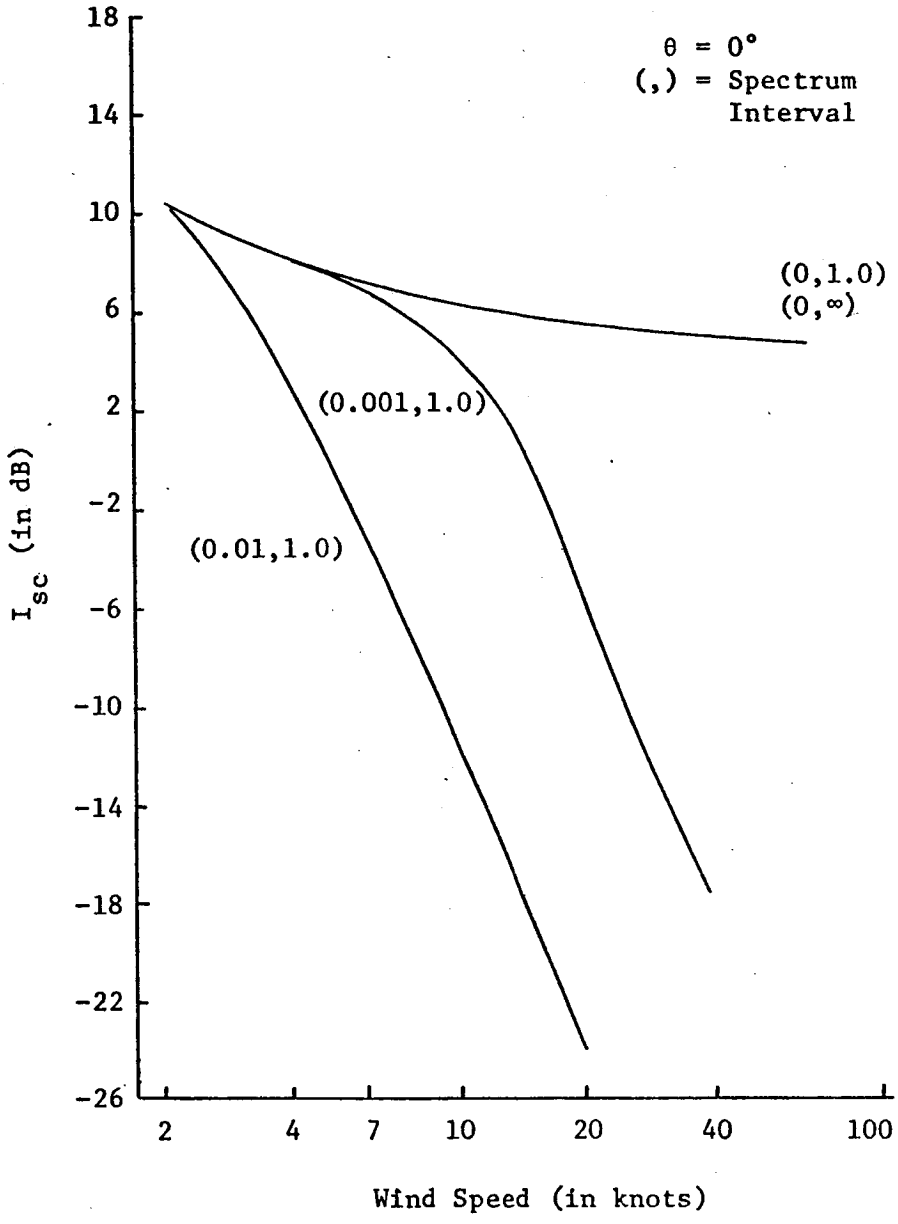

Figure 14. Behavior of scattering integral for various lower spectrum truncation points, λ_{rf} = 3 cm.

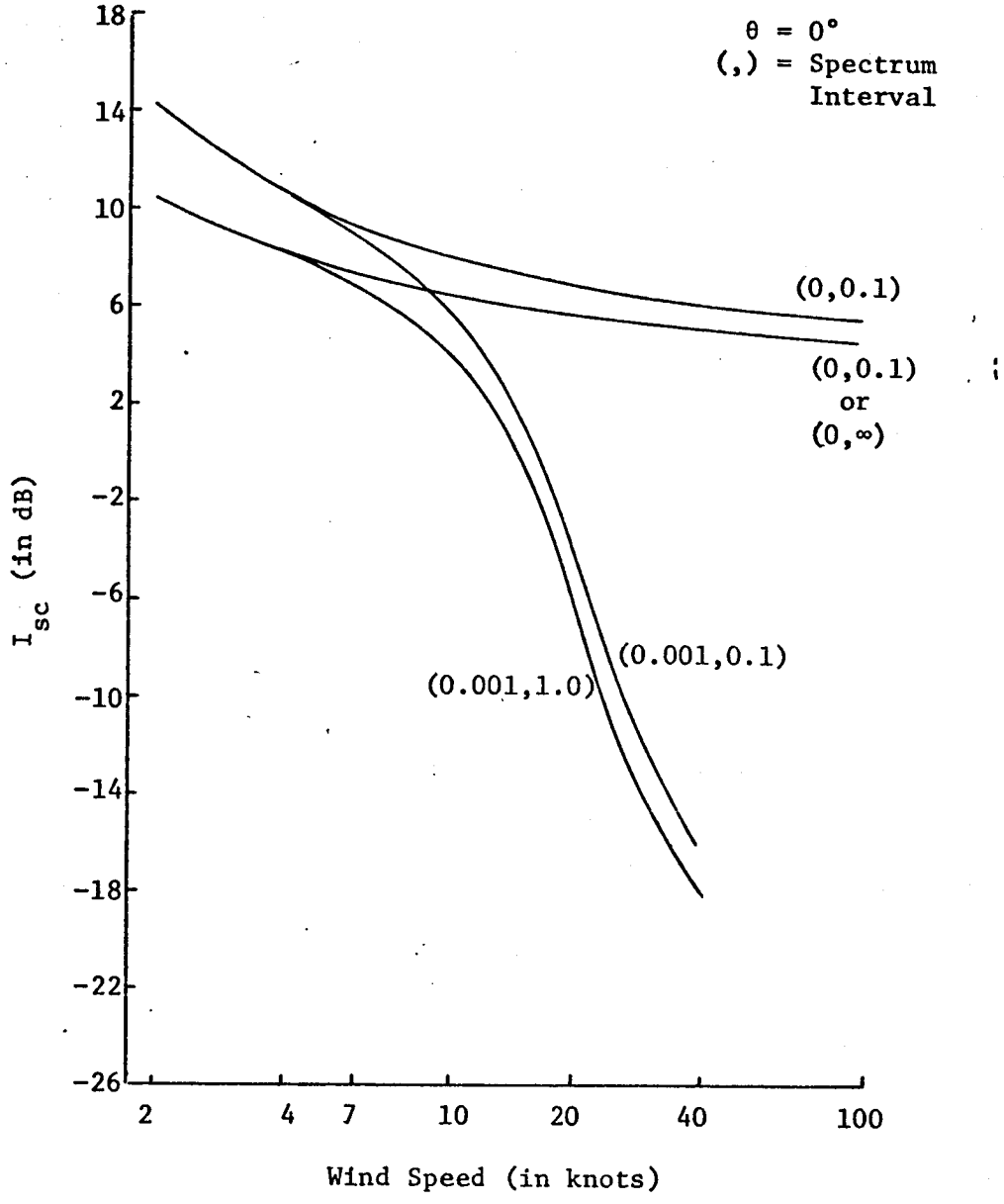

Figure 15. Behavior of scattering integral for various upper spectrum truncation points, λ_{rf} = 3 cm.